

# Optimization of 3D controlled ELM-free state with recovered global confinement for tokamak fusion plasmas

**SangKyeun Kim** (✉ [sk42@princeton.edu](mailto:sk42@princeton.edu))

Princeton University <https://orcid.org/0000-0002-0701-8962>

**Ricardo Shousha**

Princeton University

**SangHee Hahn**

Korea Institute of Fusion Energy

**Andrew Nelson**

Princeton University

**Josiah Wai**

Princeton University

**SeongMoo Yang**

Princeton Plasma Physics Laboratory

**Jong-Kyu Park**

Princeton Plasma Physics Laboratory

**Raffi Nazikian**

Princeton Plasma Physics Laboratory

**YoungMu Jeon**

Korea Institute of Fusion Energy <https://orcid.org/0000-0002-7374-3759>

**YongKyoon In**

Ulsan National Institute of Science Technology

**Jaehyun Lee**

Korea Institute of Fusion Energy

**JaeWook Kim**

Korea Institute of Fusion Energy

**ChanYoung Lee**

Seoul National University

**Yong-Su Na**

Seoul National University <https://orcid.org/0000-0001-7270-3846>

**Egemen Kolemen**

Princeton University <https://orcid.org/0000-0003-4212-3247>

---

## Article

**Keywords:** tokamak fusion plasmas, energy engineering, edge-localized modes (ELMs)

**Posted Date:** July 26th, 2021

**DOI:** <https://doi.org/10.21203/rs.3.rs-713840/v1>

**License:**  This work is licensed under a Creative Commons Attribution 4.0 International License.

[Read Full License](#)

---

<sup>1</sup> Optimization of 3D controlled ELM-free state with recovered global confinement  
<sup>2</sup> for tokamak fusion plasmas

<sup>3</sup> S.K.Kim,<sup>1</sup> R.Shousha,<sup>1</sup> S.H.Hahn,<sup>2</sup> A.O.Nelson,<sup>1</sup> J.Wai,<sup>1</sup> S.M.Yang,<sup>3</sup> J.-K.Park,<sup>3</sup>  
<sup>4</sup> R.Nazikian,<sup>3</sup> Y.M.Jeon,<sup>2</sup> Y.In,<sup>4</sup> J.H.Lee,<sup>2</sup> J.Kim,<sup>2</sup> C.Y. Lee,<sup>5</sup> Y.-S. Na,<sup>5</sup> and  
<sup>5</sup> E.Kolemen<sup>1,3</sup>

<sup>6</sup> <sup>1)</sup>*Princeton University*

<sup>7</sup> <sup>2)</sup>*Korea Institute of Fusion Energy*

<sup>8</sup> <sup>3)</sup>*Princeton Plasma Physics Laboratory*

<sup>9</sup> <sup>4)</sup>*Ulsan National Institute of Science Technology*

<sup>10</sup> <sup>5)</sup>*Seoul National University*

<sup>11</sup> (Dated: 14 July 2021)

Mitigation of deleterious heat flux from edge-localized modes (ELMs) on fusion reactors is often attempted with 3D perturbations of the confining magnetic fields. However, the established technique of resonant magnetic perturbations (RMPs) also degrades plasma performance, complicating implementation on future fusion reactors. In this paper, we introduce an adaptive real-time control scheme as a viable approach to simultaneously achieve both ELM-free states and recovered high-confinement ( $\beta_N \sim 1.91$ ,  $\beta_p \sim 1.53$ , and  $H_{98} \sim 0.9$ ), demonstrating successful handling of a volatile complex system through adaptive measures. We show that, by exploiting a salient hysteresis process to adaptively minimize the RMP strength, stable ELM suppression can be achieved while actively encouraging confinement recovery. This is made possible by a self-organized transport response in the plasma edge which reinforces the confinement improvement through a widening of the ion pedestal and promotes control stability, in contrast to the deteriorating effect on performance observed in standard RMP experiments. These results establish the real-time approach as an up-and-coming solution towards an optimized ELM-free state, which is an important step for the operation of ITER and reactor-grade tokamak plasmas. Notably, the real-time adaptive control scheme introduced here provides a path towards economic fusion reactors by maximizing the fusion gain while minimizing damage to machine components.

30 For any fusion energy source to be viable in the global marketplace, it must be able to produce  
31 large amounts of electricity without incurring significant damage on the machine. The leading ap-  
32 proach towards this goal is a tokamak run robustly in the high confinement mode (H-mode), which  
33 is characterized by a narrow edge transport barrier responsible for significantly elevated plasma  
34 pressures throughout the device<sup>1</sup>. This “pedestal” not only enhances performance in the core re-  
35 gion but also increases the non-inductive current, improving the fusion economy by reducing the  
36 external heating and recirculating power required for steady-state operation. Because of these ad-  
37 vantages, the ITER baseline scenario<sup>2</sup> plans to utilize H-mode plasmas to demonstrate ignition in  
38 a tokamak for the first time. However, H-mode also presents serious risks to reactor operation,  
39 most prominently through the creation of dangerous edge instabilities called edge localized modes  
40 (ELMs)<sup>3</sup>. These rapid relaxations of the pedestal density and temperature result in intense tran-  
41 sient heat fluxes on the reactor walls, leading to undesired material erosion and surface melting  
42 which will not be acceptable in a reactor scenario<sup>4,5</sup>. Therefore, to retain the tokamak design as a  
43 viable option for fusion reactors, it is critical that we develop methods to routinely suppress ELM  
44 events without degrading the plasma performance.

45 One of the most effective methods to control ELMs is to apply resonant magnetic perturba-  
46 tions (RMPs) using 3D coils<sup>6–9</sup>. RMPs suppress ELMs by causing additional transport<sup>10–23</sup> in  
47 the pedestal, degrading its height to a point where ELMs are no longer unstable<sup>24–26</sup>. However,  
48 this inevitably comes at the considerable expense of global confinement deterioration, decreased  
49 access to high-performance plasma regimes and thus depleted economic prospects. This degra-  
50 dation tends to be greater with a lower toroidal wave number ( $n$ ) of RMP. Even so, the use of low- $n$   
51 configurations will be important at the reactor level due to the strong decay of external fields in the  
52 thick shielding between the plasma and field coils. Undoubtedly, the compatibility of RMP ELM  
53 suppression with high confinement operation requires urgent exploration.

54 In this context, we report on an adaptive RMP scheme capable of maximizing plasma perfor-  
55 mance while maintaining robust ELM suppression. With this new technique, up to  $\sim 70\%$  of the  
56 RMP-induced performance degradation can be quickly recovered, returning the plasma to a high-  
57 power state suitable for future reactors. By exploiting a salient hysteresis process on the KSTAR  
58 tokamak<sup>27</sup>, we find that RMP-induced transport does not just produce a negative influence on  
59 confinement (as is typically assumed) but instead also opens up a pathway to strong recovery of  
60 plasma performance that is accessible to a highly-optimized controller. This leads to the concur-  
61 rent establishment of high confinement plasmas and sustained ELM suppression at normalized

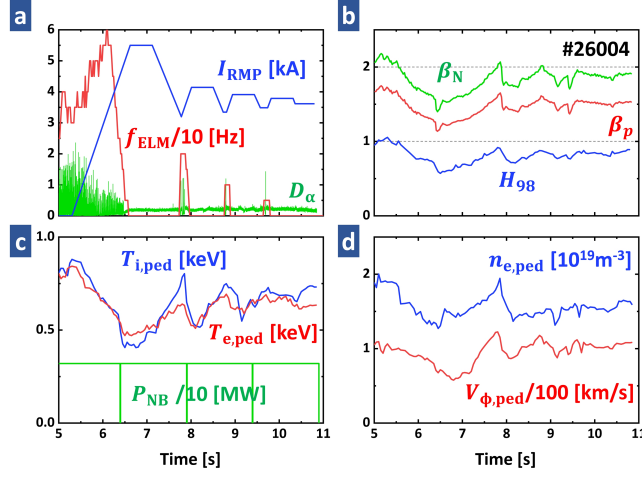


FIG. 1. **Plasma parameters for an ELM suppression discharge (#26004) with adaptive RMP control.**

**a** RMP coil current (blue),  $D_\alpha$  emission (green) near outer divertor target, and detected ELM frequency (red). **b**  $H_{98}$ (blue),  $\beta_N$  (green), and  $\beta_p$  (red). **c** Pedestal height of ion (red), electron (blue) temperature, and NBI heating power (green). **d** Pedestal height of electron density (blue) and toroidal rotation of carbon (6+) impurity (red).

62 performance close to the ITER-baseline level, reaching  $\beta_N \sim 1.91$ ,  $\beta_p \sim 1.53$ , and  $H_{98} \sim 0.9$ .  
63 Here,  $\beta_N = \frac{aB_T}{I_p} \frac{p}{B^2/2\mu_0}$  is the normalized beta,  $\beta_p = \frac{p}{B_p^2/2\mu_0}$  is the poloidal beta, and  $H_{98} = \tau_{\text{exp}}/\tau_{98}$   
64 is the thermal energy confinement quality compared to the standard H-mode plasmas, where  $p$  is  
65 the averaged plasma pressure,  $a$  is the minor radius,  $I_p$  is the total plasma,  $B_T$  is the toroidal mag-  
66 netic field,  $B_p$  is the poloidal magnetic field,  $B$  is the total magnetic field,  $\tau_{\text{exp}}$  is the experimental  
67 thermal energy confinement time, and  $\tau_{98}$  is the empirically derived confinement time using stan-  
68 dard H-mode database<sup>28</sup>. Since  $H_{98}$  enters to the power of 3.23 in determining the fusion gain  
69  $Q_{\text{fus}}$ <sup>29</sup>, where  $Q_{\text{fus}}$  is the ratio between produced fusion energy over input, the strong recovery of  
70  $H_{98}$  demonstrated in this work allows a substantial reduction of fusion cost, establishing a means  
71 with which RMPs can be used for ELM suppression to enable commercial-grade fusion devices.

## 72 I. RESULTS

73 **Optimized pedestal using adaptive control.** Figure 1 shows an example of H-mode plasma  
74 with fully suppressed ELMs via adaptive feedback RMP amplitude control. In this discharge, a  
75 hysteresis effect is utilized where ELM suppression can be maintained over long periods with a  
76 lower RMP strength than initially required for access to the ELM suppression regime<sup>17</sup>. Because

77 reduction of the RMP amplitude leads to an increased pressure pedestal height, this enables global  
78 confinement recovery in an ELM-free state<sup>30</sup> by adjusting RMP levels. To avoid ELMs while  
79 maximizing the confinement, we use a preset low  $n = 1$  RMP waveform<sup>8</sup> and apply real-time  
80 feedback to control its amplitude. During the plasma current flattop before applying RMP, with  
81  $I_p = 0.51$  MA and  $\sim 3$  MW of neutral beam injection heating,  $\beta_N \sim 2.13$ ,  $\beta_p \sim 1.71$ , and  $H_{98} \sim$   
82 1.03, close to the targets of the proposed ITER baseline scenario. In this discharge, the plasma  
83 edge safety factor  $q_{95} \sim 5$ , which is higher than the target value of  $q_{95} \sim 3$ . Here,  $q_{95}$  is defined  
84 as the pitch of the magnetic field line in the edge where the normalized poloidal flux ( $\psi_N$ ) is  
85 95%. However, after achieving the first stable ELM suppression through traditional means (7.1  
86 s), the plasma performance significantly decreases to  $\beta_N \sim 1.62$ ,  $\beta_p \sim 1.30$ , and  $H_{98} \sim 0.68$ . The  
87 30% reduction in overall confinement by RMP mainly comes from degradation in density and  
88 temperature pedestal, as shown in Fig.1c, d. Such extensive confinement and  $H_{98}$  degradation is  
89 a well-known general trend in low- $n$  RMP experiments<sup>31-33</sup> and will not be acceptable in a future  
90 fusion reactor because this leads to a significant increase in fusion cost.

91 After this initial degradation, the real-time adaptive ELM control scheme starts to recover the  
92 original performance before RMPs were introduced while maintaining stable ELM suppression.  
93 The controller leverages the  $D_\alpha$  emission signal near the outer divertor target to calculate the  
94 frequency of ELMs ( $f_{\text{ELM}}$ )<sup>34</sup>. To achieve ELM suppression, the RMP amplitude (or coil cur-  
95 rent,  $I_{\text{RMP}}$ ) is raised until  $f_{\text{ELM}}$  decreases to 0, i.e., ELM suppression. Then, during the resulting  
96 ELM-free period, the controller lowers the RMP strength to raise the pedestal height until ELMs  
97 reappear, at which point the control again starts to ramp up the RMP amplitude until suppression  
98 is recovered (Fig.1a). In the experiment presented in Fig.1, there are 0.5 s of RMP flattop intervals  
99 between the RMP-ramp up and down phase to achieve saturated RMP response. Throughout this  
100 process, we adjust the lower bound of  $I_{\text{RMP}}$  to match the value where the most recent ELM returns.  
101 This adaptive constraint reduces the likelihood of ELM suppression loss and control oscillation.  
102 The feedback system leads the plasma to a converged operating point that optimizes both ELM-  
103 free operation and confinement, recovering most of the performance lost in the initial application  
104 of RMP.

105 In the selected discharge, this adaptive ELM control scheme achieves a stable ELM-free phase  
106 at 10.5 s with improved global confinement, as shown in Fig.1b. Although a few ELMs occur  
107 before convergence, the controller successfully reaches a stable operating point with minimized  
108 ELM periods. In the final state, the plasma performance shows  $\beta_N \sim 1.91$ ,  $\beta_p \sim 1.53$ , and

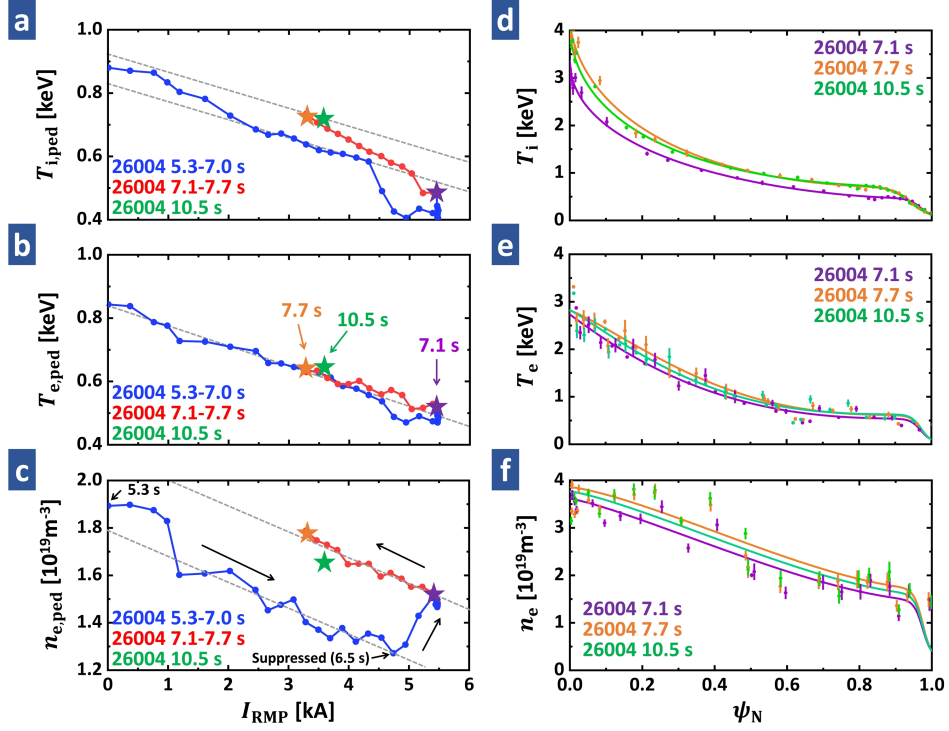


**FIG. 2. Pedestal height (left) and core plasma profiles (right) for RMP ramp-up (5.3-7.1 s, blue), down (7.1-7.7 s, red), first saturated ELM-suppression (7.1 s, purple), first optimized suppression (7.7 s, orange), and finally optimized suppression (10.5 s, green).** **a-c** Pedestal height of ion, electron temperature and electron density. **d-f** Core ion, electron temperature, and electron density with statistical error bars. Ion temperature is measured by a charge-exchange recombination system for carbon (6+) impurities. Electron temperature is measured by the Thomson Scattering and Electron cyclotron emission system. Electron density is measured by the Thomson Scattering and Two-color interferometry system.

<sup>109</sup>  $H_{98} \sim 0.9$ , recovering up to 68% of the original confinement degradation. Such increase in  $H_{98}$   
<sup>110</sup> is especially important as this leads to the 60% recovery in  $Q_{\text{fus}}$  degradation, thus emphasizing  
<sup>111</sup> the performance of adaptive control. The enhanced confinement quality occurs with the recov-  
<sup>112</sup> ery of both the temperature and density pedestals. As can be seen in Fig.1c, d, all pedestals are  
<sup>113</sup> significantly improved from the first ELM suppression phase. For example, electron ( $T_{e,\text{ped}}$ ) and  
<sup>114</sup> ion ( $T_{i,\text{ped}}$ ) temperature pedestals increase by 22% and 50%, respectively. In addition, the electron  
<sup>115</sup> density pedestal ( $n_{e,\text{ped}}$ ) is also recovered by 10% at the same time. Interestingly,  $H_{98} \sim 0.9$  at  
<sup>116</sup> 10.5 s is much larger than  $H_{98} \sim 0.75$  at 6.2 s, even with the same  $I_{\text{RMP}} = 3.6$  kA. This indicates  
<sup>117</sup> that the confinement recovery by adaptive approach is not solely attributable to decreased  $I_{\text{RMP}}$ ,  
<sup>118</sup> but rather that another contributor leads the plasma to a reinforced high-confinement state.

We note that the ion temperature pedestal exhibits significant recovery compared to the other channels. This is mainly due to the rapid and significant increase of ion pedestal height by decreasing RMP strength. The traces of pedestal height versus  $I_{RMP}$  before the first ELM re-appearance (5.3-7.7s) reveal this trend, as shown in Fig.2a-c.  $n_{e,ped}$  and  $T_{e,ped}$  have a similar dependence on  $I_{RMP}$  during the pedestal degradation (5.3-6.5s) and recovery (7.1-7.7s) phases, showing  $\frac{\Delta n_{e,ped}}{\Delta I_{RMP}} \sim -10^{15} / m^3 A$  and  $\frac{\Delta T_{e,ped}}{\Delta I_{RMP}} \sim -0.06 \text{ eV/A}$ . However,  $T_{i,ped}$  in the recovery phase shows a 50% larger response of  $-0.09 \text{ eV/A}$  compared to the degradation phase,  $-0.06 \text{ eV/A}$ . The difference of responses in these phases leads to the faster and larger recovery of the ion pedestal. As shown in Fig.2d-f, all radial profiles in the core plasma are almost identical during the recovery phase. Therefore, the improved confinement by decreasing RMP strength results from increased  $n_{e,ped}$ ,  $T_{e,ped}$ , and  $T_{i,ped}$ , with the last one dominant. In particular,  $\sim 67\%$  of improvement comes from the ion pedestal, and this is responsible for reinforced recovery by adaptive control. The large growth of  $T_{i,ped}$  is mainly due to the simultaneously increased upper limit of  $T_{i,ped}$  before the loss of ELM suppression and its enhanced response to the RMP strength. In addition,  $n_{e,ped}$  shows a large increase near  $I_{RMP} \sim 5 \text{ kA}$  (Fig.2c), which can be attributed to reduced particle pumping from ELMs. This occurs before 7 s and does not directly contribute to confinement recovery beginning at 7.1 s. However, it still strengthens the confinement recovery with increasing  $T_{i,ped}$ .

136

**Advantages of the adaptive ELM control for achieving safe ELM suppression.** In standard H-mode discharges, strong RMPs are favorable for entering the ELM suppression but also raises the possibility of dangerous plasma destabilization. Too large of an RMP field in the core plasma normally leads to a locking of plasma rotation and invokes a disastrous core instability called a disruption, as seen in Fig.3a. Core locking (or disruptions) terminate the plasma and forms transient heat fluxes on the tokamak walls which are even more severe than ELMs. Unfortunately, plasma disruption is easier with low-n RMPs. Therefore it is vital to maintain the RMP strength between the thresholds of ELM suppression and disruption. To complicate this process, these thresholds change in time with various plasma parameters and are often hard to theoretically predict. The database<sup>33</sup> for  $n = 1$  RMP ELM suppression in KSTAR reveals broadly scattered experimental thresholds showing  $1 \sim 2 \text{ kA}$  variations, and empirical prediction is also challenging due to their sensitivity to plasma parameters. For these reasons, in the present experiments, a series of discharges are used to find safe RMP strength for ELM suppression. This approach will not be applicable in a fusion reactor, where a single disruption can result in the termination of machine

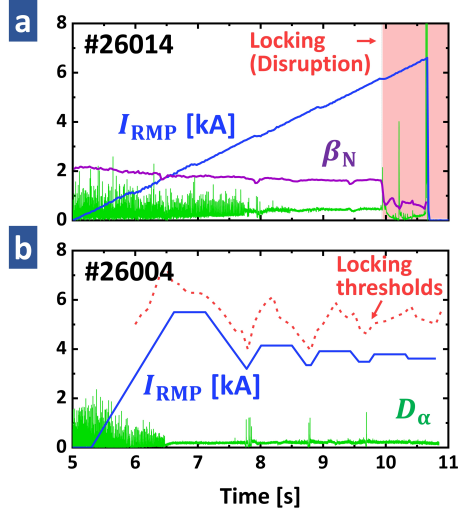


**FIG. 3. Plasma parameters for a RMP-induced disruption and suppression discharge with  $n = 1$  RMP in KSTAR. a** RMP coil current (blue),  $D_\alpha$  emission (green), and  $\beta_N$  (purple) of discharge #26014. Onset of locking (disruption) is marked as a red region. **b** RMP coil current (blue) and  $D_\alpha$  emission (green) of discharge #26004. The disruption thresholds in  $I_{RMP}$  is marked as a red dotted line.

151 life.

152 Notably, the adaptive approach lowers the RMP strength after entering the ELM-free state and  
 153 maintains it near the levels for marginally stable ELM suppression. This automatically avoids  
 154 touching the disruptive limits. As shown in Fig.3b, the RMP strength stays safely below the dis-  
 155 ruption threshold throughout the example discharge, highlighting the advantages of this adaptive  
 156 scheme for achieving stable ELM suppression. Here, the disruption thresholds are predicted from  
 157 adjacent RMP-disruption experiments and ideal RMP response calculations. Although adaptive  
 158 RMP control will be ineffective if only a small margin exists between the thresholds for suppres-  
 159 sion and disruption, it still reduces the necessity of extensive optimization of the RMP geometry  
 160 for locking avoidance, which often comes at the expense of other important parameters or opera-  
 161 tional degrees of freedom.

162

163 **Improved ELM stability and ion pedestal response by RMP-induced transports.** Instead of  
 164 causing only degradation of pedestal, RMP-induced pedestal transport facilitates the improvement  
 165 of the  $T_{i,\text{ped}}$  limit and its response to the RMP strength by broadening the ion-pedestal. RMP-  
 166 induced transport on the ion pedestal can be found from the analysis of the ion pedestal profiles in  
 167 detail. Fig.4a, b illustrate ion pedestal and  $E \times B$  flow profiles for five times between 5.3 and 7.7

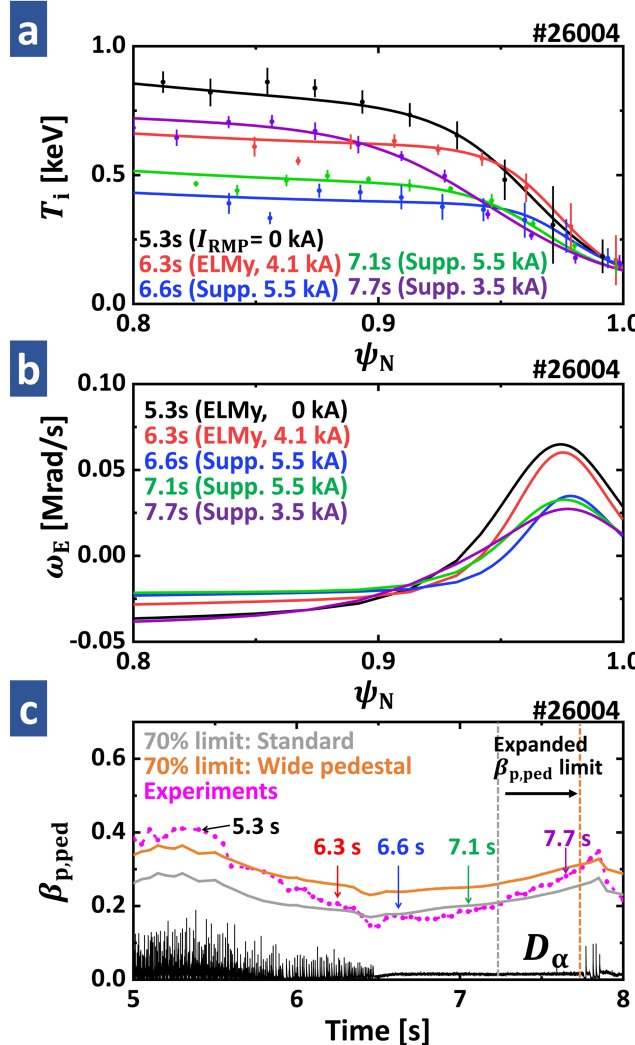


**FIG. 4. Time traces of pedestal profiles and stability limits during adaptive ELM control (#26004).** **a** Ion pedestal profiles with statistical error bars are shown for five different time slices. **b** ExB flow profiles ( $\omega_E$ ) at pedestal are shown for five different time slices. **c** 70% of ELM stability limit for  $\beta_{p,ped}$  with (orange) and without (gray) wide ion pedestal, calculated from EPED code. Experimentally measured  $\beta_{p,ped}$  (magenta) and  $D_\alpha$  emission (black) are also shown. The dotted lines show  $\beta_{p,ped}$  limits during ELM-free state imposed by pedestal stability with (gray) and without (orange) wide ion pedestal.

168 s. Before ELM suppression (5.3-6.3 s),  $T_{i,ped}$  decreases with  $I_{RMP}$ , while the pedestal gradient is  
 169 well sustained (or even slightly increased). After ELM suppression (> 6.5 s), however, the pedestal  
 170 stiffness starts to change. The transition from 6.6 to 7.1 s shows broadening of the ion pedestal and  
 171 decreasing of its gradient. This widening is maintained in the pedestal recovery phase up to 7.7  
 172 s. The decrease in pedestal height and gradient are both due to RMP-induced transport. However,

173 the rapid broadening of the ion pedestal after ELM suppression indicates that its gradient is not  
174 governed by the transport affecting the pedestal height but instead by an “additional” transport  
175 source that occurs in the ELM suppression phase.

176 The change in ion pedestal width improves the ELM stability. In theory, pedestal pressure  
177 ( $P_{\text{ped}}$ ) or pedestal poloidal beta ( $\beta_{p,\text{ped}} = \frac{P_{\text{ped}}}{B_p^2/2\mu_0}$ ) should stay under the stability limit to avoid  
178 the reappearance of ELM crashes. Stability analysis confirms that  $\beta_{p,\text{ped}}$  stays below 70% of the  
179 stability limit during the ELM suppression phase. This stability limit is known to improve with  
180 increased pedestal width<sup>35</sup>. Therefore, widened pressure pedestal via ion-pedestal broadening  
181 allows for higher  $\beta_{p,\text{ped}}$  during the ELM-free phase. Numerical analysis reveals that the  $\beta_{p,\text{ped}}$   
182 limit increases by 53% due to ion pedestal broadening. This change is presented in Fig.4c. With  
183 the expansion of the  $\beta_{p,\text{ped}}$  limit illustrated as dotted lines,  $\beta_{p,\text{ped}}$  can further increase from 0.2  
184 (gray dotted line) to 0.31 (orange dotted line). This enhanced  $\beta_{p,\text{ped}}$  limit allows access to higher  
185  $T_{i,\text{ped}}$  in the ELM suppression phase.

186 The broader ion-pedestal also can lead a larger response of  $T_{i,\text{ped}}$  on RMP strength. Inspired  
187 from (Hu et al. 2020)<sup>36</sup>, the change of pedestal height ( $\Delta T_{\text{ped}}$ ) by  $\Delta I_{\text{RMP}}$  can be described as Eq.1,

$$\frac{\Delta T_{\text{ped}}}{\Delta I_{\text{RMP}}} \approx \nabla T_{\text{ped}} \sum_{m \geq q_{\text{ped}}} \frac{\partial W_{m,n}}{\partial I_{\text{RMP}}}, \quad (1)$$

188 where  $W_{m,n}$  and  $\nabla T_{\text{ped}}$  are the  $(m,n)$  island width and pedestal gradient, respectively.  $q_{\text{ped}}$  is an  
189 edge safety factor on the pedestal top. This expression is based on the concept where  $\Delta T_{\text{ped}}$  is  
190 the accumulation of profile flattening by the islands in the pedestal region. We note that constant  
191  $\nabla T_{\text{ped}}$  over the pedestal region is assumed to make interpretation easier. This expression addresses  
192 that pedestal height changes more rapidly with RMP strength as the pedestal gradient grows and  
193  $q_{\text{ped}}$  decreases. With the given  $q$  profile monotonic,  $q_{\text{ped}}$  is reduced by increasing pedestal width.  
194 The largely broadened ion pedestal can lead to a stronger response of  $T_{i,\text{ped}}$  despite the decrease of  
195 ion pedestal gradient. In addition, ion pedestal is known to be heavily influenced by neoclassical  
196 transport<sup>15,37,38</sup>. Here, neoclassical heat flux by RMPs is roughly proportional to  $I_{\text{RMP}}^2$ , and it  
197 increases more rapidly with the smaller radial electric field and its gradient<sup>39,40</sup>. Because a wide  
198 ion pedestal reduces the electric field<sup>19,41</sup> at the pedestal (Fig.4b), this correlation also contributes  
199 to improving the response of  $T_{i,\text{ped}}$ .

200 On the other hand, the responses of  $n_{e,\text{ped}}$  and  $T_{e,\text{ped}}$  to RMP strength are almost identical  
201 whether or not the ELMs are fully suppressed. This means that additional RMP-induced transport  
202 in the ELM-free phase has a smaller effect on the electron density and temperature pedestal gra-

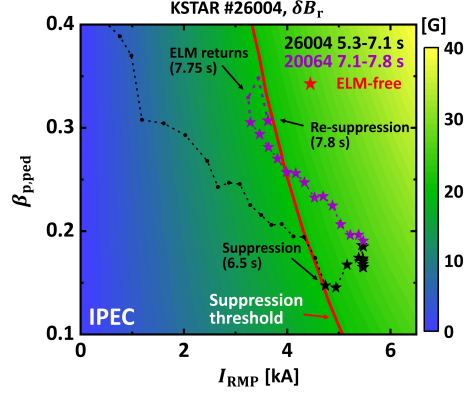


FIG. 5. The pressure pedestal height versus RMP strength during adaptive ELM control (#26004).

The time traces of  $\beta_{p,ped}$  in #26004 discharge for 5.3-7.1 s (black) and 7.1-7.8 s (purple) with varying  $I_{RMP}$ . ELM-free states are marked as star dots. Contours of  $\delta B_r$  at pedestal region from ideal response calculation using IPEC are also shown. Experimentally derived  $\delta B_r$  threshold for ELM suppression is drawn as a red curve.

203 dient. Although the electron pedestal width has considerable uncertainty due to limitations in the  
 204 resolution of edge diagnostics, its value lies between 4-6% in normalized poloidal flux without  
 205 showing a considerable widening like ion pedestal, suggesting that additional transport has only a  
 206 relatively small effect on electron channels.

207

208 **Advantages of RMP-induced transport and wide ion pedestal in adaptive ELM control.** In-  
 209 creased  $T_{i,ped}$  response by RMP-induced transport leads to an extensive recovery of  $T_{i,ped}$  during  
 210 RMP ramp-down and makes an ion pedestal higher than the RMP ramp-up phase (ELMy) even  
 211 with the same RMP strength. In addition, enhanced pedestal stability allows for larger  $T_{i,ped}$  before  
 212 the return of ELMs. The synergy between these effects boosts the pedestal recovery and enables  
 213 adaptive control to maximize the confinement, resulting in a much higher pedestal than during the  
 214 initial phase of ELM suppression, as shown in Fig.5, which illustrates  $\beta_{p,ped}$  versus  $I_{RMP}$ . The  
 215 changes to the pedestal from 5.3 to 7.8 s are shown, and the ELM suppressed states are marked  
 216 with star points.

217 Another advantage of RMP-induced transport is that it improves the control stability. Adaptive  
 218 control can be unstable due to a bifurcation of the plasma state during transitions between ELMy  
 219 and ELM-free regimes, which causes oscillation of the control system. In particular, it can take  
 220 a long time or even become impossible for a controller to find the optimal solution because of

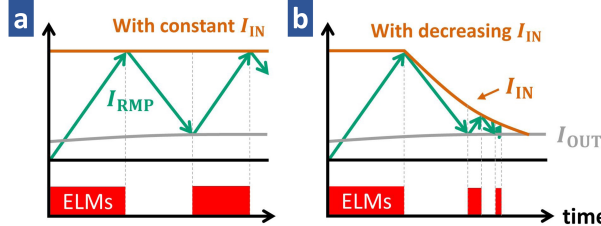


**FIG. 6. Schematic diagram of adaptive ELM control using RMPs.** Here, RMP threshold for ELM suppression entry ( $I_{IN}$ , orange) and exit ( $I_{OUT}$ , gray) are drawn. Time trace of  $I_{RMP}$  (green) and onset of ELMs (red box) are also shown. Expected time trace of adaptive ELM control with **a** constant  $I_{IN}$  and **b** decreasing  $I_{IN}$  in time.

the sudden jump in RMP strength required for re-entry ( $I_{IN}$ ) to or exit ( $I_{OUT}$ ) from ELM suppression. The schematic diagram in Fig.6a illustrates how this characteristic will delay the control convergence. In practice, ELM control must be done quickly to minimize damage to the reactor, so an adaptive approach is generally hard to use in such a bifurcating system. However, RMP-induced transport eases these control difficulties by reducing  $I_{IN}$  during adaptive control, as shown in Fig.6b.

It has been shown that the plasma enters the ELM suppression state above a certain  $\delta B_r$  threshold<sup>42</sup>, where  $\delta B_r$  is the perturbed radial field strength at the pedestal. This threshold ( $\sim 20$  G) for the reference discharge is shown as the red contour of Fig.5. Here,  $\beta_{p,ped}$  amplifies the perturbed field<sup>42</sup>, and the same  $\delta B_r$  can be obtained with a smaller  $I_{RMP}$  with larger  $\beta_{p,ped}$ . Because RMP-induced transport enhances  $\beta_{p,ped}$  in an ELM-free state, this leads to a lower  $I_{IN}$ , making access to the next ELM suppression regime easier. The ELM suppression of 7.8 s shown in Fig.5 results from reduced  $I_{IN}$  compared to the former one at 6.5 s. Thus,  $I_{IN}$  for each suppression entry changes as  $4.9 \rightarrow 3.6 \rightarrow 3.53 \rightarrow 3.5$  kA, as seen in Fig.1(a), resulting in fast and stable system optimization. This interesting example shows uncommon *positive effect*<sup>43,44</sup> of self-organized transport on pedestal confinement.

We note that such an RMP-induced hysteresis shown in Fig5 is not trivial to be produced in the experiment as it conventionally requires a delicate pre-programmed RMP waveform. This leads to difficulties in investigating and exploiting the hysteresis, which is critical to optimize the ELM-free state. In this respect, adaptive RMP control is an effective methodology as it can automatically generate the hysteresis and utilize it. In addition, the adaptive scheme has been successfully operated for more than a hundred confinement times ( $\sim 5$  s) of KSTAR, and therefore,

<sup>243</sup> this control is also expected to be applicable to long pulse plasma in ITER.

<sup>244</sup>

<sup>245</sup> **The origin of broadened ion-peDESTAL.** It is worth pointing out that successful adaptive con-  
<sup>246</sup> trol in these experiments is mainly due to a broadened ion pedestal during the ELM suppression  
<sup>247</sup> phase. As shown in Fig.7a, the ion heat diffusivity ( $\chi_i$ ) of the pedestal region rapidly increases  
<sup>248</sup> via additional transport after transitions to the ELM-free state. In addition, the pedestal heat dif-  
<sup>249</sup> fusivity does not change much during 7.1-7.7 s, indicating that it is insensitive to the decreasing  
<sup>250</sup>  $I_{RMP}$ . It has been reported that the neoclassical transport effect dominates ion heat transport under  
<sup>251</sup> RMPs<sup>37,38</sup>. However, this collisional transport strongly depends on the RMP strength. There-  
<sup>252</sup> fore, the broadened ion pedestal does not seem to be related to the neoclassical process. Here,  
<sup>253</sup>  $\chi_i$  at  $\psi_N = 0.96$  exceeds neoclassical level ( $\geq 0.4\text{m}^2/\text{s}$ ) in all cases, supporting the existence of  
<sup>254</sup> additional transport.

<sup>255</sup> Fluctuation measurements on KSTAR ( $k_y \rho_s < 0.1$ ) reveal significant edge turbulence triggered  
<sup>256</sup> by RMPs<sup>25,26,45</sup> after ELM suppression, where  $k_y$  is the bi-normal wave number,  $\rho_s = \sqrt{2m_i T_e}/eB$   
<sup>257</sup> is the hybrid Larmor radius, and  $m_i$  is deuterium mss. Fig.7c, d illustrate the spectrogram and the  
<sup>258</sup> coherence strength of  $\delta T_e$  and  $\delta n_e$  fluctuations at  $\psi_N \sim 0.96$ . Fig.7e shows the poloidal magnetic  
<sup>259</sup> field fluctuations ( $\delta B_{pol}$ ) at the inner wall. Here,  $\delta T_e$  and  $\delta n_e$  have strong coherence over the  
<sup>260</sup> frequency range of 20-100 kHz. The magnetic fluctuations in the 80-400 kHz range are also  
<sup>261</sup> observed during the same period. As shown in Fig.7f, they show an immediate instigation of  
<sup>262</sup> turbulence as ELM suppression begins followed by quick saturation within 200 ms. We note that  
<sup>263</sup> coherence before 6.4 s comes from ELM noise, and a magnetic signal of <50 kHz is responsible  
<sup>264</sup> for core modes. It is noteworthy that the strength of coherent fluctuations remains almost identical  
<sup>265</sup> during 7.1-7.7 s. Here, the widening of the ion pedestal coincides with the occurrence of edge  
<sup>266</sup> fluctuations. Furthermore, they are both insensitive to RMP strength. Therefore, these similarities  
<sup>267</sup> support the claim that the ion pedestal is widened primarily due to increased heat diffusivity by  
<sup>268</sup> edge turbulence.

<sup>269</sup> Linear gyrokinetic simulations confirms that enhanced edge turbulence may occur in the ELM  
<sup>270</sup> suppression phase. As shown in Fig.7b, the linear growth rates ( $\gamma/\gamma_E$ ) of turbulence mode exceed  
<sup>271</sup> the onset limit (>1) after the transitions to the ELM-free state. This is mainly due to decreased  
<sup>272</sup> stabilizing effect from the ExB shearing rate ( $\gamma_E$ )<sup>46,47</sup>, which comes from the degraded pressure  
<sup>273</sup> pedestal (Fig.4b). It turns out that the excited modes are correlated with the ITG/TEM hybrid.  
<sup>274</sup> Here, the bi-normal wave length  $k_y \rho_s \sim 0.3$  and real frequency  $\sim 51$  kHz of the most unstable

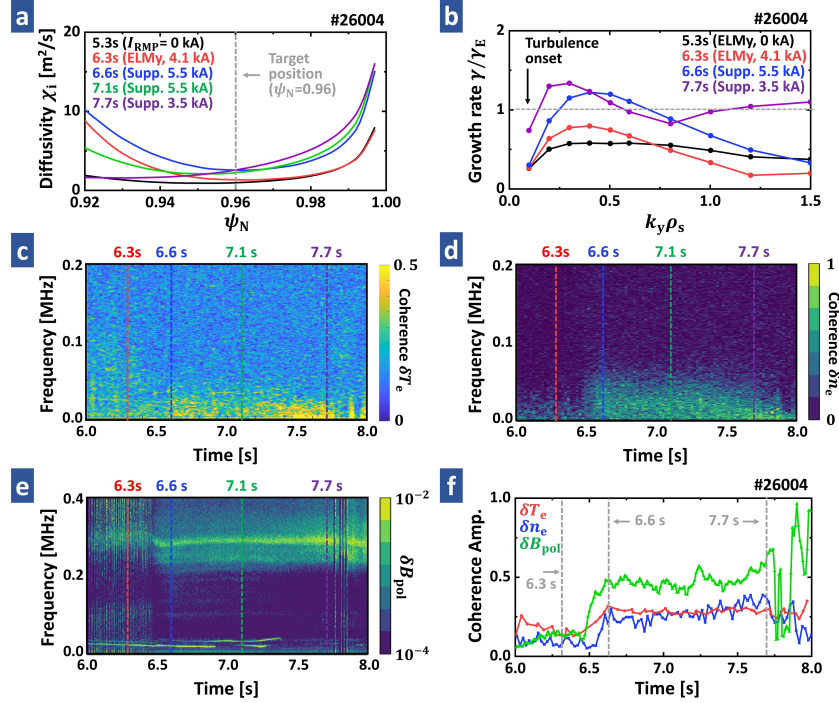


**FIG. 7. A broadened ion temperature pedestal by RMP-induced transport during ELM-suppression state.** **a** Radial profiles of ion heat diffusivity ( $\chi_i$ ) for five different time slices. **b** The growth rates of instability calculated from Gyro-kinetic simulation code CGYRO. **c** Coherence of edge  $T_e$  fluctuation from Electron cyclotron emission imaging system. **d** Coherence of edge  $n_e$  fluctuation from Beam emission imaging system. **e** Measured  $\delta B_{pol}$  fluctuation at inner wall from Mirnov coil. **f** Time trace of normalized integrated coherence amplitude of  $T_e$  (red),  $n_e$  (blue), and  $B_{pol}$  (green) fluctuations over the frequency space.

mode exhibits similar properties to the measured fluctuations of electron channels. The simulation results show that ion thermal diffusion can be increased with these unstable modes, supporting the idea of ion pedestal broadening by turbulence. However, theoretical analysis on RMP-induced turbulence still has many missing pieces. Recent studies have shown that the characteristics of transport in the presence of RMP deviates significantly from linear gyrokinetic calculations, raising the importance of non-linearity<sup>48</sup> and non-locality<sup>49</sup>. In the future, nonlinear gyrokinetic studies including these effects will shed further light on the accurate description of edge turbulence under RMPs.

The considerable effect of RMP-induced transport on ion heat diffusion might inconsistent with the general trend of other devices<sup>16,17,32</sup>, where such turbulence mainly affects electron channel and has a minor effect on ion transport. Although it is difficult to evaluate the turbulence effect

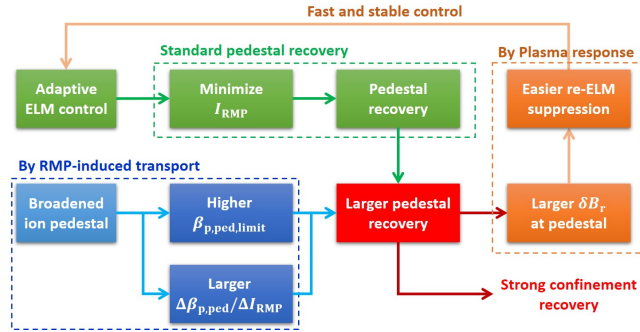


**FIG. 8. Schematic diagram of correlation between adaptive ELM control and pedestal recovery.** Here, it is noteworthy that the strong recovery of confinement is also attributable to the widened ion pedestal by RMP-induced transport during ELM suppression phase.

286 on  $n_e$  and  $T_e$  due to limitations in the diagnostics, we still confirm that there is a clear correlation  
 287 between edge fluctuation and ion pedestal. Therefore, this observation suggests new possible role  
 288 of turbulence on the ion pedestal under the low- $n (= 1)$  RMP and ELM-free states.

## 289 II. DISCUSSION

290 We have achieved successful optimization of a controlled ELM-free state with highly recov-  
 291 ered confinement by  $\sim 60\%$ , maintaining  $\beta_N \sim 1.91$ ,  $\beta_p \sim 1.53$ , and  $H_{98} \sim 0.9$ , with the original  
 292 degradation in fusion gain largely recovered. This novel adaptive approach exhibits compatibility  
 293 between RMP ELM suppression and high confinement. In addition, it provides a reliable strategy  
 294 to achieve stable ELM-free access by preventing RMP-induced disruption. It is noteworthy that  
 295 the remarkable recovery of confinement is not solely attributable to adaptive RMP control but also  
 296 to a widened ion pedestal resulting from RMP-induced transport that promotes pedestal recovery  
 297 by improving the ion response and ELM stability and facilitates fast, stable, and reinforced control  
 298 optimization (Fig.8). This feature, which can be correlated to the turbulent process, is a good ex-  
 299 ample of a system that transitions to an optimal state through a self-organized response to adaptive  
 300 modulation. These results with low  $n = 1$  RMP confirm that adaptive ELM control is a highly  
 301 promising approach towards optimizing the ELM-free state, potentially solving one of the most  
 302 challenging obstacles for viable and economical fusion energy.

303 However, there are remaining features to be improved for a “complete” adaptive ELM control  
 304 picture. As shown in Fig.1a, the current approach is based on ELM detection and thereby in-

305 inevitably faces several ELMs during control. This limitation could be critical at the reactor level,  
306 where a single ELM can already be dangerous. Thus, a way to detect the loss of ELM suppression  
307 in advance of the ELM re-occurrence is needed. Here, the behavior of edge turbulence suggests  
308 the potential solution. The amplitude of magnetic fluctuation during the ELM-free phase shows a  
309 rapid decrease 70 ms before the return of ELMs at 7.75 s (Fig.7f). Such an abrupt change in mag-  
310 netic signals is an effective indicator of suppression loss. Therefore, this property can be utilized  
311 in real-time to entirely avoid the return of ELM to achieve truly ELM-free optimization.

312 Previous work has shown that the effectiveness of RMP ELM suppression can be enhanced by  
313 physics model-based 3D geometric optimization<sup>50</sup>. Since this adaptive ELM control scheme max-  
314 imizes the plasma performance for a given scenario, any additional improvements from external  
315 forces will be augmented by the adaptive scheme. This makes the adaptive approach a prime can-  
316 didate to fully exploit existing physics models for RMP ELM suppression. Future integration of  
317 these features will lead to broader operational freedom and higher confinement recovery, as well  
318 as the development of advanced ELM control techniques for ITER and future tokamaks.

### 319 III. METHODS

320 **KSTAR tokamak.** The KSTAR tokamak is the largest magnetic fusion devices in Republic of  
321 Korea, supported by the Korea Institute of Fusion Energy (KFE) and the Government funds. It has  
322 the plasma major radius  $R_0 = 1.8$  m, minor radius  $a_0 = 0.45$  m, and the toroidal magnetic field  
323  $B_T = 1.8 - 2.3$  T at major radius  $R_0$ . The  $n = 1$  RMP ELM suppression discharge on KSTAR can  
324 be reproduced at a lower electron density regime (.e.g., Greenwald density fraction  $\sim 0.4$ ) with a  
325 plasma shape having elongation  $\kappa \sim 1.71$ , upper triangularity  $\delta_{\text{up}} \sim 0.37$ , and upper triangularity  
326  $\delta_{\text{low}} \sim 0.85$ .

327

328 **Radial profile reconstruction.** Core ion temperature is measured by charge exchange recombi-  
329 nation system<sup>51</sup> for Carbon (6+) impurities at outboard mid-plane. Core electron temperature is  
330 measured by the Thomson Scattering<sup>52</sup> and Electron Cyclotron emission<sup>53</sup> system. Core electron  
331 density is measured by the Thomson Scattering and Two-color interferometry system<sup>54</sup>. To obtain  
332 well-resolved profiles, the data are averaged over 100 ms. The pedestal height is obtained from  
333 hyperbolic tangent fits with edge profiles. The equilibria from EFIT code<sup>55</sup> is used for the radial  
334 profile mapping and fitting.

335

336 **Kinetic equilibria reconstruction.** Kinetic equilibria are reconstructed for the plasma stability  
337 analysis. This equilibrium is calculated from the magnetic reconstruction using EFIT code with  
338 the pressure profile (summation of thermal pressure profile from radial profile reconstruction and  
339 fast ion pressure from NUBEAM code<sup>56</sup>) and current density profile (core current from motional  
340 Stark effect diagnostics<sup>57</sup> and edge current using NUBEAM, Ohmic and Sauter current models<sup>58</sup>)  
341 as a constraint. An iteration scheme is employed to update the thermal profiles, NUBEAM results,  
342 and edge current calculation with new kinetic equilibrium.

343

344 **Pedestal stability calculation.** The pedestal stability (or ELM stability) limit is predicted using  
345 the EPED<sup>159</sup> algorithm. The fixed-boundary equilibrium code, CHEASE<sup>60</sup>, is used for accurate  
346 equilibrium mapping, and the ideal MHD stability code, MISHKA1<sup>61</sup>, is employed for ideal  
347 peeling-balloonning<sup>3</sup> stability calculation. The linear initial value solver is used to calculate the  
348 most unstable mode. All other required parameters are taken from the reconstructed radial profiles  
349 and plasma equilibrium.

350

351 **Ideal plasma response calculation.** The perturbed radial fields ( $\delta B_r$ ) from an ideal plasma re-  
352 sponse by RMP are calculated using IPEC code<sup>62</sup> and given magnetic equilibria and  $I_{RMP}$ . The  
353 core and edge responses are derived through radially averaging  $\delta B_r$  at  $\psi_N = 0 - 0.9$  and  $0.9 - 1.0$ ,  
354 respectively. The thresholds of  $\delta B_r$  for RMP-induced ELM suppression and disruption are ob-  
355 tained from neighboring experiments. The disruption thresholds in  $I_{RMP}$  are equivalent to the  $\delta B_r$   
356 thresholds based on the plasma response calculation.

357

358 **Plasma fluctuation measurements.** In this work, edge  $T_e$  and  $n_e$  fluctuations ( $k_{\perp} \rho < 1$ ) are  
359 measured from electron emission image spectroscopy (ECEI)<sup>63</sup> and beam emission spectroscopy  
360 (BES)<sup>64</sup>, respectively. Magnetic field perturbations are captured by the Mirnov coil signal (MC)<sup>65</sup>.  
361 The spectrogram of measured fluctuation is derived using Fourier transform. Coherence of elec-  
362 tron density and temperature fluctuation is calculated from bi-spectrum analysis with two radially  
363 adjacent channels in ECEI and BES, respectively. The ELM peaks and core modes are statistically  
364 removed from integrating the amplitude of coherent fluctuations in all channels.

365

366 **Gyro-kinetic simulation.** The gyrokinetic code, CGYRO<sup>66</sup>, is used in the linear analysis of

<sup>367</sup> micro-instabilities. The linear initial value solver is employed to find the unstable mode in the  
<sup>368</sup> target radial point with wavelength  $k_y \rho_s = 0.1 - 1.5$ . This simulation is based on a flux-tube ap-  
<sup>369</sup> proach with a full gyro-kinetic description for both electron and ion channels. The reconstructed  
<sup>370</sup> radial profiles and kinetic equilibrium described above are included for the accurate modeling.  
<sup>371</sup> This calculation is performed at  $\psi_N = 0.96$ , where the changes of experimental fluctuations are  
<sup>372</sup> robust.

<sup>373</sup>

#### <sup>374</sup> IV. ACKNOWLEDGMENTS

<sup>375</sup> The authors would like to thanks KSTAR team. This material was supported by the U.S. Depart-  
<sup>376</sup> ment of Energy, under Awards DE-SC0020372. This research was also supported by R&D Pro-  
<sup>377</sup> gram of "KSTAR Experimental Collaboration and Fusion Plasma Research(EN2021-12)" through  
<sup>378</sup> the Korea Institute of Fusion Energy(KFE) funded by the Government funds.

#### <sup>379</sup> V. AUTHOR CONTRIBUTIONS

<sup>380</sup> S.K. and R.S. led the experimental demonstration and analysis. R.S. and S.K. develop the adaptive  
<sup>381</sup> controller. E.K. conceived the original idea of adaptive control. A.O.N. analyzed the micro insta-  
<sup>382</sup> bility with Gyro-kinetic code. S.H., S.Y., J.W. and Y.M. participated in all the experimental pro-  
<sup>383</sup> cedures and support the analysis. R.N. and Y.I. discussed the critical physics picture of ion-scale  
<sup>384</sup> turbulence and other transports at the pedestal. J.P. and Y.S. discussed the role of RMP response,  
<sup>385</sup> stability and transport analysis of pedestal region. C.Y conducted the interpretive transport analy-  
<sup>386</sup> sis using ASTRA. J.L. and J.K. analyzed the measured edge fluctuation in electron channel. S.K.  
<sup>387</sup> wrote the main manuscript text and A.O.N. and all authors reviewed it.

#### <sup>388</sup> VI. ADDITIONAL INFORMATION

<sup>389</sup> Competing financial interests: The authors declare no competing financial interests.

390 REFERENCES

- 391 <sup>1</sup>F. Wagner, G. Fussmann, T. Grave, M. Keilhacker, M. Kornherr, K. Lackner, K. McCormick,  
392 E. R. Müller, A. Stäbler, G. Becker, K. Bernhardi, U. Ditte, A. Eberhagen, O. Gehre, J. Gern-  
393 hardt, G. v. Gierke, E. Glock, O. Gruber, G. Haas, M. Hesse, G. Janeschitz, F. Karger, S. Kissel,  
394 O. Klüber, G. Lisitano, H. M. Mayer, D. Meisel, V. Mertens, H. Murmann, W. Poschenrieder,  
395 H. Rapp, H. Röhr, F. Ryter, F. Schneider, G. Siller, P. Smeulders, F. Söldner, E. Speth, K. H.  
396 Steuer, Z. Szymanski, and O. Vollmer, en“Development of an Edge Transport Barrier at the  
397 H-Mode Transition of ASDEX,” Physical Review Letters **53**, 1453–1456 (1984).
- 398 <sup>2</sup>A. Sips, J. Schweinzer, T. Luce, S. Wolfe, H. Urano, J. Hobirk, S. Ide, E. Joffrin, C. Kessel,  
399 S. Kim, P. Lomas, I. Nunes, T. Pütterich, F. Rimini, W. Solomon, J. Stober, F. Turco, P. de Vries,  
400 JET Contributors, The ASDEX Upgrade team, The DIII-D team, The C-Mod team, The JT-60U  
401 team, and ITPA-IOS TG members and experts, en“Assessment of the baseline scenario at  $q_{95}$   
402  $\sim 3$  for ITER,” Nuclear Fusion **58**, 126010 (2018).
- 403 <sup>3</sup>J. W. Connor, R. J. Hastie, H. R. Wilson, and R. L. Miller, en“Magnetohydrodynamic stability  
404 of tokamak edge plasmas,” Physics of Plasmas **5**, 2687–2700 (1998).
- 405 <sup>4</sup>A. Loarte, G. Huijsmans, S. Futatani, L. Baylor, T. Evans, D. M. Orlov, O. Schmitz, M. Becoulet,  
406 P. Cahyna, Y. Gribov, A. Kavin, A. Sashala Naik, D. Campbell, T. Casper, E. Daly, H. Frerichs,  
407 A. Kischner, R. Laengner, S. Lisgo, R. Pitts, G. Saibene, and A. Wingen, en“Progress on the  
408 application of ELM control schemes to ITER scenarios from the non-active phase to DT opera-  
409 tion,” Nuclear Fusion **54**, 033007 (2014).
- 410 <sup>5</sup>J. Gunn, S. Carpentier-Chouchana, F. Escourbiac, T. Hirai, S. Panayotis, R. Pitts, Y. Corre,  
411 R. Dejarnac, M. Firdaouss, M. Kočan, M. Komm, A. Kukushkin, P. Languille, M. Missirlian,  
412 W. Zhao, and G. Zhong, en“Surface heat loads on the ITER divertor vertical targets,” Nuclear  
413 Fusion **57**, 046025 (2017).
- 414 <sup>6</sup>T. E. Evans, R. A. Moyer, P. R. Thomas, J. G. Watkins, T. H. Osborne, J. A. Boedo, E. J. Doyle,  
415 M. E. Fenstermacher, K. H. Finken, R. J. Groebner, M. Groth, J. H. Harris, R. J. L. Haye, C. J.  
416 Lasnier, S. Masuzaki, N. Ohyabu, D. G. Pretty, T. L. Rhodes, H. Reimerdes, D. L. Rudakov,  
417 M. J. Schaffer, G. Wang, and L. Zeng, “Suppression of Large Edge-Localized Modes in High-  
418 Confinement DIII-D Plasmas with a Stochastic Magnetic Boundary,” Physical Review Letters  
419 **92** (2004), 10.1103/physrevlett.92.235003, publisher: American Physical Society (APS).

- <sup>420</sup> <sup>7</sup>W. Suttrop, T. Eich, J. C. Fuchs, S. Günter, A. Janzer, A. Herrmann, A. Kallenbach, P. T. Lang,  
<sup>421</sup> T. Lunt, M. Maraschek, R. M. McDermott, A. Mlynek, T. Pütterich, M. Rott, T. Vierle, E. Wol-  
<sup>422</sup> frum, Q. Yu, I. Zammuto, and H. Zohm, en“First Observation of Edge Localized Modes Mit-  
<sup>423</sup> igation with Resonant and Nonresonant Magnetic Perturbations in ASDEX Upgrade,” Physical  
<sup>424</sup> Review Letters **106**, 225004 (2011).
- <sup>425</sup> <sup>8</sup>Y. M. Jeon, J.-K. Park, S. W. Yoon, W. H. Ko, S. G. Lee, K. D. Lee, G. S. Yun, Y. U. Nam, W. C.  
<sup>426</sup> Kim, J.-G. Kwak, K. S. Lee, H. K. Kim, and H. L. Yang, “Suppression of Edge Localized Modes  
<sup>427</sup> in High-Confinement KSTAR Plasmas by Nonaxisymmetric Magnetic Perturbations,” Physical  
<sup>428</sup> Review Letters **109** (2012), 10.1103/physrevlett.109.035004, publisher: American Physical So-  
<sup>429</sup> ciety (APS).
- <sup>430</sup> <sup>9</sup>Y. Sun, Y. Liang, Y. \.e. Liu, S. Gu, X. Yang, W. Guo, T. Shi, M. Jia, L. Wang, B. Lyu, C. Zhou,  
<sup>431</sup> A. Liu, Q. Zang, H. Liu, N. Chu, H. \.e. Wang, T. Zhang, J. Qian, L. Xu, K. He, D. Chen,  
<sup>432</sup> B. Shen, X. Gong, X. Ji, S. Wang, M. Qi, Y. Song, Q. Yuan, Z. Sheng, G. Gao, P. Fu, and  
<sup>433</sup> B. Wan, “Nonlinear Transition from Mitigation to Suppression of the Edge Localized Mode  
<sup>434</sup> with Resonant Magnetic Perturbations in the EAST Tokamak,” Physical Review Letters **117**  
<sup>435</sup> (2016), 10.1103/physrevlett.117.115001, publisher: American Physical Society (APS).
- <sup>436</sup> <sup>10</sup>M. E. Fenstermacher, T. E. Evans, T. H. Osborne, M. J. Schaffer, M. P. Aldan, J. S. deGrassie,  
<sup>437</sup> P. Gohil, I. Joseph, R. A. Moyer, P. B. Snyder, R. J. Groebner, M. Jakubowski, A. W. Leonard,  
<sup>438</sup> O. Schmitz, and the DIII-D Team, en“Effect of island overlap on edge localized mode suppres-  
<sup>439</sup> sion by resonant magnetic perturbations in DIII-D,” Physics of Plasmas **15**, 056122 (2008).
- <sup>440</sup> <sup>11</sup>F. L. Waelbroeck, I. Joseph, E. Nardon, M. Bécoulet, and R. Fitzpatrick, “Role of singular layers  
<sup>441</sup> in the plasma response to resonant magnetic perturbations,” Nuclear Fusion **52**, 074004 (2012),  
<sup>442</sup> publisher: IOP Publishing.
- <sup>443</sup> <sup>12</sup>Q. M. Hu, R. Nazikian, B. A. Grierson, N. C. Logan, J.-K. Park, C. Paz-Soldan, and Q. Yu, “The  
<sup>444</sup> density dependence of edge-localized-mode suppression and pump-out by resonant magnetic  
<sup>445</sup> perturbations in the DIII-D tokamak,” Physics of Plasmas **26**, 120702 (2019), publisher: AIP  
<sup>446</sup> Publishing.
- <sup>447</sup> <sup>13</sup>R. Fitzpatrick, “Theory of edge localized mode suppression by static resonant magnetic pertur-  
<sup>448</sup> bations in the DIII-D tokamak,” Physics of Plasmas **27**, 042506 (2020), publisher: AIP Publish-  
<sup>449</sup> ing.
- <sup>450</sup> <sup>14</sup>Y. Liu, C. Paz-Soldan, L. Li, and Y. Sun, en“Role of 3D neoclassical particle flux in density  
<sup>451</sup> pump-out during ELM control by RMP in DIII-D,” Nuclear Fusion **60**, 036018 (2020).

- 452 15 V. Rozhansky, P. Molchanov, E. Kaveeva, S. Voskoboinikov, A. Kirk, E. Nardon, D. Coster, and  
453 M. Tendler, en “Modelling of the edge plasma of MAST in the presence of resonant magnetic  
454 perturbations,” Nuclear Fusion **51**, 083009 (2011).
- 455 16 S. Mordijk, R. A. Moyer, and G. R. McKee, en “Changes in density fluctuations as a result  
456 of resonant magnetic perturbations correlate with the density inverse scale length,” Physics of  
457 Plasmas **19**, 024504 (2012).
- 458 17 G. McKee, Z. Yan, C. Holland, R. Buttery, T. Evans, R. Moyer, S. Mordijk, R. Nazikian,  
459 T. Rhodes, O. Schmitz, and M. Wade, en “Increase of turbulence and transport with resonant  
460 magnetic perturbations in ELM-suppressed plasmas on DIII-D,” Nuclear Fusion **53**, 113011  
461 (2013).
- 462 18 H. Müller, T. Lunt, W. Suttrop, T. Eich, R. Fischer, J. Fuchs, A. Herrmann, M. Kočan,  
463 P. de Marné, and E. Wolfrum, en “Modification of scrape-off layer transport and turbulence by  
464 non-axisymmetric magnetic perturbations in ASDEX Upgrade,” Journal of Nuclear Materials  
465 **438**, S64–S71 (2013).
- 466 19 N. Vianello, C. Rea, M. Agostini, R. Cavazzana, G. Ciaccio, G. De Masi, E. Martines, A. Mazzi,  
467 B. Momo, G. Spizzo, P. Scarin, M. Spolaore, P. Zanca, M. Zuin, L. Carraro, P. Innocente,  
468 L. Marrelli, M. E. Puiatti, and D. Terranova, en “Magnetic perturbations as a viable tool for  
469 edge turbulence modification,” Plasma Physics and Controlled Fusion **57**, 014027 (2015).
- 470 20 C. Rea, N. Vianello, M. Agostini, R. Cavazzana, G. De Masi, E. Martines, B. Momo, P. Scarin,  
471 S. Spagnolo, G. Spizzo, M. Spolaore, and M. Zuin, en “Comparative studies of electrostatic tur-  
472 bulence induced transport in presence of resonant magnetic perturbations in RFX-mod,” Nuclear  
473 Fusion **55**, 113021 (2015).
- 474 21 L. Cui, R. Nazikian, B. Grierson, E. Belli, T. Evans, N. Logan, D. Orlov, S. Smith, G. Staebler,  
475 and P. Snyder, en “The energy confinement response of DIII-D plasmas to resonant magnetic  
476 perturbations,” Nuclear Fusion **57**, 116030 (2017).
- 477 22 S. Liu, N. Yan, Y. Liang, H. Zhang, J. Xu, G. Xu, L. Wang, R. Chen, G. Hu, Y. Ye, Y. Sun, T. Shi,  
478 H. Wang, M. Wu, X. Wu, S. Gu, M. Jia, N. Chu, Q. Ma, Y. Wang, T. Zhang, X. Han, L. Chen,  
479 J. Liu, S. Xu, H. Wang, N. Zhao, W. Zhang, J. Qian, L. Zeng, L. Xu, S. Wang, H. Liu, Q. Zang,  
480 Y. Yu, L. Liao, X. Gong, and EAST, en “Edge turbulence characteristics and transport during  
481 the ELM mitigation with  $n = 1$  resonant magnetic perturbation on EAST,” Nuclear Fusion **60**,  
482 082001 (2020).

- 483   <sup>23</sup>M. W. Jakubowski, T. E. Evans, M. E. Fenstermacher, M. Groth, C. J. Lasnier, A. W. Leonard,  
484   O. Schmitz, J. G. Watkins, T. Eich, W. Fundamenski, R. A. Moyer, R. C. Wolf, L. B. Bay-  
485   lor, J. A. Boedo, K. H. Burrell, H. Frerichs, J. S. deGrassie, P. Gohil, I. Joseph, S. Mordijk,  
486   M. Lehnert, C. C. Petty, R. I. Pinsker, D. Reiter, T. L. Rhodes, U. Samm, M. J. Schaffer, P. B.  
487   Snyder, H. Stoschus, T. Osborne, B. Unterberg, E. Unterberg, and W. P. West, “Overview of the  
488   results on divertor heat loads in RMP controlled H-mode plasmas on DIII-D,” Nuclear Fusion  
489   **49**, 095013 (2009), publisher: IOP Publishing.
- 490   <sup>24</sup>P. Snyder, K. Burrell, H. Wilson, M. Chu, M. Fenstermacher, A. Leonard, R. Moyer, T. Osborne,  
491   M. Umansky, W. West, and X. Xu, en“Stability and dynamics of the edge pedestal in the low  
492   collisionality regime: physics mechanisms for steady-state ELM-free operation,” Nuclear Fusion  
493   **47**, 961–968 (2007).
- 494   <sup>25</sup>R. Nazikian, C. Paz-Soldan, J. \. e. Callen, J. \. e. deGrassie, D. Eldon, T. \. e. Evans, N. \. e.  
495   Ferraro, B. \. e. Grierson, R. \. e. Groebner, S. \. e. Haskey, C. \. e. Hegna, J. \. e. King, N. \. e.  
496   Logan, G. \. e. McKee, R. \. e. Moyer, M. Okabayashi, D. \. e. Orlov, T. \. e. Osborne, J.-K.  
497   Park, T. \. e. Rhodes, M. \. e. Shafer, P. \. e. Snyder, W. \. e. Solomon, E. \. e. Strait, and  
498   M. \. e. Wade, “Pedestal Bifurcation and Resonant Field Penetration at the Threshold of Edge-  
499   Localized Mode Suppression in the DIII-D Tokamak,” Physical Review Letters **114** (2015),  
500   10.1103/physrevlett.114.105002, publisher: American Physical Society (APS).
- 501   <sup>26</sup>C. Paz-Soldan, R. Nazikian, S. \. e. Haskey, N. \. e. Logan, E. \. e. Strait, N. \. e. Ferraro, J. \. e.  
502   Hanson, J. \. e. King, M. \. e. Lanctot, R. \. e. Moyer, M. Okabayashi, J.-K. Park, M. \. e.  
503   Shafer, and B. \. e. Tobias, “Observation of a Multimode Plasma Response and its Relation-  
504   ship to Density Pumpout and Edge-Localized Mode Suppression,” Physical Review Letters **114**  
505   (2015), 10.1103/physrevlett.114.105001, publisher: American Physical Society (APS).
- 506   <sup>27</sup>G. Lee, J. Kim, S. Hwang, C. Chang, H. Chang, M. Cho, B. Choi, K. Kim, K. Cho, S. Cho,  
507   K. Choh, C. Choi, J. Choi, J. Choi, I. Choi, C. Do, T. Ha, J. Han, J. Hong, K. Hong, N. Hur,  
508   I. Hwang, K. Im, H. Jhang, Y. Jung, B. Kim, D. Kim, G. Kim, H. Kim, J. Kim, J. Kim, W. Kim,  
509   Y. Kim, K. Kwon, M. Kyum, B. Lee, D. Lee, H. Lee, J. Lee, S. Lee, H. Na, Y. Oh, J. Park,  
510   H. Ri, Y. Ryoo, K. Song, H. Yang, J. Yang, B. Yoo, S. Yoo, N. Yoon, S. Yoon, G. You, K. You,  
511   W. Choe, D.-I. Choi, S. Jeong, D. Lee, Y. Bae, H. Kang, G. Kim, I. Ko, W. Namkung, J. Oh,  
512   Y. Bae, Y. Cho, B. Hong, G. Hong, C. Hwang, S. In, M. Ju, H. Lee, B. Oh, B. Yoon, S. Baang,  
513   H. Choi, J. Hwang, M. Kim, Y. Kim, S. Lee, J. Yee, C. Yoon, K.-H. Chung, S. Hong, Y. Hwang,  
514   S. Kim, Y. Kim, K. Chung, J. Lim, D. Ha, S. Oh, K. Ryu, Q. Wang, T. Ko, J. Joo, S. Suh, C. Choi,

- 515 J. Lee, Y. Lee, H. Shin, I. Song, J. Baek, I. Han, Y. Koh, P. Park, C. Ryu, J. Cho, D. Hwang,  
516 Y. Kim, J. Schmidt, H. Park, G. Neilson, W. Reiersen, R. Simmons, S. Bernabei, F. Dahlgren,  
517 L. Grisham, S. Jardin, C. Kessel, J. Manickam, S. Medley, N. Pomphrey, J. Sinnis, T. Brown,  
518 R. White, K. Young, J. Schultz, P. Wang, L. Sevier, M. Carter, P. Ryan, D. Swain, D. Hill,  
519 W. Nevins, and B. Braams, en “The KSTAR project: An advanced steady state superconducting  
520 tokamak experiment,” Nuclear Fusion **40**, 575–582 (2000).
- 521 <sup>28</sup>I. P. E. G. o. C. Transport, I. P. E. G. o. C. Database, and I. P. B. Editors, “Chapter 2: Plasma  
522 confinement and transport,” Nuclear Fusion **39**, 2175–2249 (1999).
- 523 <sup>29</sup>H. Zohm, en “On the Minimum Size of DEMO,” Fusion Science and Technology **58**, 613–624  
524 (2010).
- 525 <sup>30</sup>F. Laggner, D. Eldon, A. Nelson, C. Paz-Soldan, A. Bortolon, T. Evans, M. Fenstermacher,  
526 B. Grierson, Q. Hu, D. Humphreys, A. Hyatt, R. Nazikian, O. Meneghini, P. Snyder, E. Unter-  
527 berg, E. Kolemen, and t. DIII-D team, en “Real-time pedestal optimization and ELM control  
528 with 3D fields and gas flows on DIII-D,” Nuclear Fusion **60**, 076004 (2020).
- 529 <sup>31</sup>Y. In, J.-K. Park, Y. M. Jeon, J. Kim, G. Y. Park, J.-W. Ahn, A. Loarte, W. H. Ko, H. H. Lee, J. W.  
530 Yoo, J. W. Juhn, S. W. Yoon, and H. P. and, “Enhanced understanding of non-axisymmetric in-  
531 trinsic and controlled field impacts in tokamaks,” Nuclear Fusion **57**, 116054 (2017), publisher:  
532 IOP Publishing.
- 533 <sup>32</sup>C. Sung, G. Wang, T. L. Rhodes, S. P. Smith, T. H. Osborne, M. Ono, G. R. McKee, Z. Yan, R. J.  
534 Groebner, E. M. Davis, L. Zeng, W. A. Peebles, and T. E. Evans, en “Increased electron temper-  
535 ature turbulence during suppression of edge localized mode by resonant magnetic perturbations  
536 in the DIII-D tokamak,” Physics of Plasmas **24**, 112305 (2017).
- 537 <sup>33</sup>M. Kim, J. Lee, W. H. Ko, S.-H. Hahn, Y. In, Y. M. Jeon, W. Sutrop, S. K. Kim, G. Y. Park, J.-W.  
538 Juhn, and J. H. Lee, en “Pedestal electron collisionality and toroidal rotation during ELM-crash  
539 suppression phase under  $n = 1$  RMP in KSTAR,” Physics of Plasmas **27**, 112501 (2020).
- 540 <sup>34</sup>D. Eldon, E. Kolemen, J. Barton, A. Briesemeister, D. Humphreys, A. Leonard, R. Maingi,  
541 M. Makowski, A. McLean, A. Moser, and P. Stangeby, en “Controlling marginally detached  
542 divertor plasmas,” Nuclear Fusion **57**, 066039 (2017).
- 543 <sup>35</sup>T. Osborne, G. Jackson, Z. Yan, R. Maingi, D. Mansfield, B. Grierson, C. Chrobak, A. McLean,  
544 S. Allen, D. Battaglia, A. Briesemeister, M. Fenstermacher, G. McKee, P. Snyder, and The  
545 DIII-D Team, “Enhanced H-mode pedestals with lithium injection in DIII-D,” Nuclear Fusion  
546 **55**, 063018 (2015).

- <sup>547</sup> <sup>36</sup>Q. Hu, R. Nazikian, B. Grierson, N. Logan, D. Orlov, C. Paz-Soldan, and Q. Yu, en“Wide Operational Windows of Edge-Localized Mode Suppression by Resonant Magnetic Perturbations in the DIII-D Tokamak,” Physical Review Letters **125**, 045001 (2020).
- <sup>550</sup> <sup>37</sup>V. Rozhansky, E. Kaveeva, P. Molchanov, I. Veselova, S. Voskoboynikov, D. Coster, A. Kirk, S. Lisgo, and E. Nardon, en“Modification of the edge transport barrier by resonant magnetic perturbations,” Nuclear Fusion **50**, 034005 (2010).
- <sup>553</sup> <sup>38</sup>E. Viezzer, M. Cavedon, P. Cano-Megias, E. Fable, E. Wolfrum, D. J. Cruz-Zabala, P. David, R. Dux, R. Fischer, G. F. Harrer, F. M. Laggner, R. M. McDermott, U. Plank, T. Pütterich, M. Willensdorfer, and the ASDEX Upgrade Team, en“Dynamics of the pedestal transport during edge localized mode cycles at ASDEX Upgrade,” Plasma Physics and Controlled Fusion **62**, 024009 (2020).
- <sup>558</sup> <sup>39</sup>W. A. Houlberg, K. C. Shaing, S. P. Hirshman, and M. C. Zarnstorff, en“Bootstrap current and neoclassical transport in tokamaks of arbitrary collisionality and aspect ratio,” Physics of Plasmas **4**, 3230–3242 (1997).
- <sup>561</sup> <sup>40</sup>S. Mordijk, R. Moyer, N. Ferraro, M. Wade, and T. Osborne, en“The radial electric field as a measure for field penetration of resonant magnetic perturbations,” Nuclear Fusion **54**, 082003 (2014).
- <sup>564</sup> <sup>41</sup>J. Lee, Y. M. Jeon, Y. In, G. Y. Park, G. S. Yun, W. Lee, M. Kim, J. H. Lee, W. H. Ko, and H. K. P. and, “Direct evidence of  $E \times B$  flow changes at the onset of resonant magnetic perturbation-driven edge-localized mode crash suppression,” Nuclear Fusion **59**, 066033 (2019), publisher: IOP Publishing.
- <sup>568</sup> <sup>42</sup>J.-K. Park, Y. Jeon, Y. In, J.-W. Ahn, R. Nazikian, G. Park, J. Kim, H. Lee, W. Ko, H.-S. Kim, N. C. Logan, Z. Wang, E. A. Feibusch, J. E. Menard, and M. C. Zarnstroff, “3D field phase-space control in tokamak plasmas,” Nature Physics **14**, 1223–1228 (2018), publisher: Springer Science and Business Media LLC.
- <sup>572</sup> <sup>43</sup>X. Chen, K. Burrell, T. Osborne, W. Solomon, K. Barada, A. Garofalo, R. Groebner, N. Luhmann, G. McKee, C. Muscatello, M. Ono, C. Petty, M. Porkolab, T. Rhodes, J. Rost, P. Snyder, G. Staebler, B. Tobias, Z. Yan, and the DIII-D Team, en“Stationary QH-mode plasmas with high and wide pedestal at low rotation on DIII-D,” Nuclear Fusion **57**, 022007 (2017).
- <sup>576</sup> <sup>44</sup>R. Nazikian, C. Petty, A. Bortolon, X. Chen, D. Eldon, T. Evans, B. Grierson, N. Ferraro, S. Haskey, M. Knolker, C. Lasnier, N. Logan, R. Moyer, D. Orlov, T. Osborne, C. Paz-Soldan, F. Turco, H. Wang, and D. Weisberg, en“Grassy-ELM regime with edge resonant magnetic

- 579 perturbations in fully noninductive plasmas in the DIII-D tokamak," Nuclear Fusion **58**, 106010  
580 (2018).
- 581 <sup>45</sup>J. Lee, G. S. Yun, M. J. Choi, J.-M. Kwon, Y.-M. Jeon, W. Lee, N. C. Luhmann, and  
582 H. K. Park, "Nonlinear Interaction of Edge-Localized Modes and Turbulent Eddies in Toroidal  
583 Plasma under  $\eta=1$ Magnetic Perturbation," Physical Review Letters **117** (2016), 10.1103/phys-  
584 revlett.117.075001, publisher: American Physical Society (APS).
- 585 <sup>46</sup>H. Biglari, P. H. Diamond, and P. W. Terry, "Influence of sheared poloidal rotation on edge  
586 turbulence," Physics of Fluids B: Plasma Physics **2**, 1–4 (1990), publisher: AIP Publishing.
- 587 <sup>47</sup>T. S. Hahm and K. H. Burrell, "Flow shear induced fluctuation suppression in finite aspect ratio  
588 shaped tokamak plasma," Physics of Plasmas **2**, 1648–1651 (1995), publisher: AIP Publishing.
- 589 <sup>48</sup>R. Hager, C. S. Chang, N. M. Ferraro, and R. Nazikian, en "Gyrokinetic understanding of the  
590 edge pedestal transport driven by resonant magnetic perturbations in a realistic divertor geom-  
591 etry," Physics of Plasmas **27**, 062301 (2020), arXiv: 2003.07130.
- 592 <sup>49</sup>S. Taimourzadeh, L. Shi, Z. Lin, R. Nazikian, I. Holod, and D. Spong, en "Effects of RMP-  
593 induced changes of radial electric fields on microturbulence in DIII-D pedestal top," Nuclear  
594 Fusion **59**, 046005 (2019).
- 595 <sup>50</sup>S. Yang, J.-K. Park, N. Logan, C. Zhu, Q. Hu, Y. Jeon, Y. In, W. Ko, S. Kim, Y. Lee, and  
596 Y. Na, "Localizing resonant magnetic perturbations for edge localized mode control in KSTAR,"  
597 Nuclear Fusion **60**, 096023 (2020).
- 598 <sup>51</sup>Won-Ha Ko, Seungtae Oh, and Myeon Kwon, en "KSTAR Charge Exchange Spectroscopy Sys-  
599 tem," IEEE Transactions on Plasma Science **38**, 996–1000 (2010).
- 600 <sup>52</sup>J. H. Lee, S. Oh, H. M. Wi, W. R. Lee, K. P. Kim, K. team, I. Yamada, K. Narihara, and  
601 K. Kawahata, en "Tangential Thomson scattering diagnostic for the KSTAR tokamak," Journal  
602 of Instrumentation **7**, C02026–C02026 (2012).
- 603 <sup>53</sup>G. S. Yun, W. Lee, M. J. Choi, J. B. Kim, H. K. Park, C. W. Domier, B. Tobias, T. Liang,  
604 X. Kong, N. C. Luhmann, and A. J. H. Donné, en "Development of KSTAR ECE imaging  
605 system for measurement of temperature fluctuations and edge density fluctuations," Review of  
606 Scientific Instruments **81**, 10D930 (2010).
- 607 <sup>54</sup>K. Lee, J.-W. Juhn, Y. Nam, Y. Kim, H. Wi, S. Kim, and Y.-c. Ghim, en "The design of two color  
608 interferometer system for the 3-dimensional analysis of plasma density evolution on KSTAR,"  
609 Fusion Engineering and Design **113**, 87–91 (2016).

- 610   <sup>55</sup>L. Lao, H. St. John, R. Stambaugh, A. Kellman, and W. Pfeiffer, en“Reconstruction of current  
611   profile parameters and plasma shapes in tokamaks,” Nuclear Fusion **25**, 1611–1622 (1985).
- 612   <sup>56</sup>A. Pankin, D. McCune, R. Andre, G. Bateman, and A. Kritz, en“The tokamak Monte Carlo fast  
613   ion module NUBEAM in the National Transport Code Collaboration library,” Computer Physics  
614   Communications **159**, 157–184 (2004).
- 615   <sup>57</sup>J. Chung, J. Ko, J. Howard, C. Michael, G. v. Nessi, A. Thorman, and M. F. M. D. Bock,  
616   “Motional Stark effect diagnostics for KSTAR,” Journal of the Korean Physical Society **65**,  
617   1257–1260 (2014), publisher: Korean Physical Society.
- 618   <sup>58</sup>O. Sauter, C. Angioni, and Y. R. Lin-Liu, en“Neoclassical conductivity and bootstrap current  
619   formulas for general axisymmetric equilibria and arbitrary collisionality regime,” Physics of  
620   Plasmas **6**, 2834–2839 (1999).
- 621   <sup>59</sup>P. B. Snyder, R. J. Groebner, A. W. Leonard, T. H. Osborne, and H. R. Wilson, en“Development  
622   and validation of a predictive model for the pedestal height,” Physics of Plasmas **16**, 056118  
623   (2009).
- 624   <sup>60</sup>H. Lütjens, A. Bondeson, and O. Sauter, “The CHEASE code for toroidal MHD equilibria,”  
625   Computer Physics Communications **97**, 219–260 (1996), publisher: Elsevier BV.
- 626   <sup>61</sup>A. Mikhailovskii, G. Huysmans, W. Kerner, and S. Sharapov, “Optimization of computational  
627   MHD normal-mode analysis for tokamaks,” Plasma Physics Reports **23**, 844–857 (1997).
- 628   <sup>62</sup>J.-k. Park, A. H. Boozer, and A. H. Glasser, en“Computation of three-dimensional tokamak and  
629   spherical torus equilibria,” Physics of Plasmas **14**, 052110 (2007).
- 630   <sup>63</sup>G. S. Yun, W. Lee, M. J. Choi, J. Lee, M. Kim, J. Leem, Y. Nam, G. H. Choe, H. K. Park,  
631   H. Park, D. S. Woo, K. W. Kim, C. W. Domier, N. C. Luhmann, N. Ito, A. Mase, and S. G. Lee,  
632   “Quasi 3D ECE imaging system for study of MHD instabilities in KSTAR,” Review of Scientific  
633   Instruments **85**, 11D820 (2014), publisher: AIP Publishing.
- 634   <sup>64</sup>Y. U. Nam, S. Zoretnik, M. Lampert, Kovácsik, and H. M. Wi, en“Edge electron density profiles  
635   and fluctuations measured by two-dimensional beam emission spectroscopy in the KSTAR,”  
636   Review of Scientific Instruments **85**, 11E434 (2014).
- 637   <sup>65</sup>J. G. Bak, S. G. Lee, D. Son, and the KSTAR Project Team, en“Performance of the magnetic  
638   sensor and the integrator for the KSTAR magnetic diagnostics,” Review of Scientific Instruments  
639   **75**, 4305–4307 (2004).
- 640   <sup>66</sup>J. Candy, E. Belli, and R. Bravenec, en“A high-accuracy Eulerian gyrokinetic solver for colli-  
641   sional plasmas,” Journal of Computational Physics **324**, 73–93 (2016).